INTERNATIONAL JOURNAL FOR NUMERICAL METHODS IN FLUIDS, 12, 179–195 (1991)

A FINITE ELEMENT SOLUTION TO TURBULENT DIFFUSION IN A CONVECTIVE BOUNDARY LAYER

PRASAD PAI AND T. H. TSANG

Department of Chemical Engineering, University of Kentucky, Lexington, KY 40506-0046, U.S.A.

SUMMARY

A second-order closure turbulence model is used to simulate the plume behaviour of a passive contaminant dispersed in a convective boundary layer. A time-splitting finite element scheme is used to solve the set of partial differential equations. It is shown that the second-order closure model compares favourably with recent findings from laboratories, wind-tunnel experiments and large-eddy simulations. We also compare the second-order closure model with the commonly used K-diffusion model for the same meteorological conditions. Case studies also show the effects of model parameters and turbulence variables on the plume behaviour.

KEY WORDS Air pollution modelling Turbulent diffusion Convective boundary layer Second-order closure Time-splitting finite element

INTRODUCTION

Dispersion of contaminants in convective (daytime) boundary layers is a significant problem in air pollution and accidental release of hazardous chemicals in the atmosphere. Much progress has been made in recent years towards the fundamental understanding of this problem. The pioneering work of Deardorff and Willis[1] and Willis and Deardorff[2–4] showed rather surprising plume behaviour in convective boundary layers. For the case of near-ground emission the plume 'lifts off' from the ground and forms an elevated maximum concentration close to the inversion layer, whereas for the case of elevated sources the plume 'descends' and forms a local maximum at ground level at a certain downwind distance. These laboratory data were further confirmed by wind-tunnel experiments[5] and field data.[6]

Modelling attempts of atmospheric turbulence and diffusion fall into two categories. First, the Reynolds time-averaging approach leads to the formation of higher-order correlation terms. Thus there are more unknowns than the number of transport equations. In order to deal with this closure problem, the higher correlation terms are approximated by the dependent variables and their gradients. This procedure leads to a heirarchy of turbulence models. Today, the simplest and the most commonly used model in air pollution studies is the K-diffusion model (also called the atmospheric diffusion model), which is a first-order closure model. Secondly, the volume-averaging approach of Deardorff[7] leads to large-eddy simulation (LES). The filtered momentum, material and energy balance equations are solved with the use of first- or second-order closure models for subgrid scale motions. Therefore, as the grid size increases, the volume-averaging method used in LES approaches the time-averaging method. Ordinarily, LES is more computationally intensive. However, it has been proved that LES can provide detailed turbulence structures as evidenced by the recent work of Moeng[8] and Nieuwstadt and De Valk.[9]

0271–2091/91/020179–17$08.50

Received 2 June 1989
Revised 28 December 1989

In this paper we show quantitatively that the K-diffusion model cannot describe the plume behaviour in convective boundary layers. We use Lewellen and Teske's second-order closure model,[10] which is based on Donaldson's approach,[11] to calculate turbulence variables. Once calculated, they are used in the cross-wind integrated transport equations. This allows us to study the effects of turbulence variables and their model constants on the plume behaviour and to compare our results with the second-order closure models of Enger[12] and Sun.[13] A time-splitting finite element method is used to solve the set of cross-wind integrated transport equations. In principle, the second-order closure model and the finite element method can be extended to three-dimensional problems. However, in order to validate the model, we use the 2D cross-wind transport equations because most laboratory data and simulation results provide cross-wind integrated concentration contours.

THE SECOND-ORDER CLOSURE MODEL

The two-dimensional cross-wind integrated transport equations for the dispersion of passive contaminants in a convective boundary layer have been derived by Enger[12] and Sun[13] and will not be repeated here. They are as follows:

$$\frac{\partial C_y}{\partial t}+U\frac{\partial C_y}{\partial x}=-\frac{\partial \overline{wc_y}}{\partial z}, \tag{1}$$

$$\frac{\partial \overline{wc_y}}{\partial t}+U\frac{\partial \overline{wc_y}}{\partial x}=-\overline{uw}\frac{\partial C_y}{\partial x}-\overline{ww}\frac{\partial C_y}{\partial z}+\frac{\partial}{\partial z}\left(2\Lambda_2 q\frac{\partial \overline{wc_y}}{\partial z}\right)+\frac{\partial}{\partial z}\left(\Lambda_3 q\frac{\partial \overline{wc_y}}{\partial z}\right)$$
$$-\left(\frac{Aq}{\Lambda}\right)\overline{wc_y}+\left(\frac{g}{\Theta}\right)\overline{c\theta_y}, \tag{2}$$

$$\frac{\partial \overline{c\theta_y}}{\partial t}+U\frac{\partial \overline{c\theta_y}}{\partial x}=-\overline{wc_y}\frac{\partial \Theta}{\partial z}-\overline{w\theta}\frac{\partial C_y}{\partial z}+\frac{\partial}{\partial z}\left(\Lambda_2 q\frac{\partial \overline{c\theta_y}}{\partial z}\right)-\left(\frac{2bsq}{\Lambda}\right)\overline{c\theta_y}, \tag{3}$$

where x is the prevailing (mean) wind direction and z is the vertical height from the ground. U is the wind velocity in the x-direction, Θ is the virtual potential temperature, q $(=\overline{u_i u_i}^{1/2})$ is the turbulent velocity, $\overline{uw}$ is the vertical momentum flux, $\overline{ww}$ is the vertical velocity variance and $\overline{w\theta}$ is the vertical heat flux. These variables are functions of z, the vertical height above ground level. g is the acceleration due to gravity. The length scales Λ, Λ_2 and Λ_3 are due to parametrizations of the higher-order terms. A, b and s are model constants. The choice of length scales and model constants will de discussed later. The cross-wind integrated concentration C_y is defined as

$$C_y=\int_{-\infty}^{\infty} C\,\mathrm{d}y.$$

$\overline{wc_y}$ and $\overline{c\theta_y}$ are the cross-wind integrated concentration flux and the cross-wind integrated covariance of concentration and temperature respectively, defined as

$$\overline{wc_y}=\int_{-\infty}^{\infty}\overline{wc}\,\mathrm{d}y, \qquad \overline{c\theta_y}=\int_{-\infty}^{\infty}\overline{c\theta}\,\mathrm{d}y.$$

The left-hand side of equations (1)–(3) contain the temporal derivatives and the advection terms of the three unknown variables. The first two terms on the right-hand side of equations (2) and (3) are the production terms due to the interaction with the mean field. The third term on the right-

hand side of equations (2) and (3) is the parameterization for the gradients of the third-order correlation. The fourth and fifth terms on the right-hand side of equation (2) are the model representation of the pressure diffusion term and the tendency-towards-isotropy term respectively. The last term on the right-hand side of equation (2) is the buoyancy production term. The last term on the right-hand side of equation (3) is the parameterization of the dissipation term for the covariance of concentration and temperature.[10]

The mean wind velocity U and the mean potential temperature Θ were obtained from the simulated data at 14:00 EST during day 33 of the Wangara experiments. At that time the convective boundary layer was fully developed with an inversion height $z_i = 1100$ m. The turbulence fields of meteorological variables, which include $\overline{uw}$, $\overline{ww}$, q and $\overline{w\theta}$, were calculated from a one-dimensional model based on Donaldson's approach with the assumption of horizontal homogeneity. The detailed equations of this second-order closure model to determine the turbulence variables are given in the Appendix.

A Gaussian distribution for C_y was used as the boundary condition:

$$C_y(\bar{x}, z) = \frac{Q}{\sqrt{(2\pi)}\sigma_z(\bar{x})U_s}\left[\exp\left(\frac{-(z_s-z)^2}{2\sigma_z^2(\bar{x})}\right)+\exp\left(\frac{-(z_s+z)^2}{2\sigma_z^2(\bar{x})}\right)\right], \tag{4}$$

where $\bar{x}$ is the downwind distance at which the boundary condition is applied. This is done to avoid singularity at $x=0$. Thus the values for the cross-wind integrated concentration calculated by equation (4) at $\bar{x}=200$ m are the boundary values for the simulation.

$$\sigma_z(\bar{x}) = \overline{ww}^{1/2}\bar{x}/U_s \tag{5}$$

is the vertical standard deviation at a distance $\bar{x}$, z_s is the source height, U_s is the wind speed at the source height and Q is the source strength.

The boundary condition for $\overline{wc_y}$ at $\bar{x}=200$ m is

$$\overline{wc_y} = -K_h(\mathrm{d}C_y/\mathrm{d}z), \tag{6}$$

where the eddy coefficients are assumed as

$$K_h = 3\,K_m \quad \text{for unstable stratification,} \tag{7}$$

$$K_h = K_m \quad \text{for stable stratification,} \tag{8}$$

$$K_m = 0{\cdot}1\,\Lambda\sqrt{E}. \tag{9}$$

Here K_m and K_h are the eddy coefficients for momentum and heat respectively and $E\,(=\frac{1}{2}q^2)$ is the turbulent kinetic energy. The use of equations (7) and (8) is common practice.[14,15]

The boundary conditions in the vertical direction are

$$\partial C_y/\partial z = 0, \qquad \partial\overline{wc_y}/\partial z = 0, \qquad \partial\overline{c\theta_y}/\partial z = 0 \tag{10}$$

at the top of the boundary and

$$\partial C_y/\partial z = 0, \qquad \overline{wc_y} = 0, \qquad \overline{c\theta_y} = 0 \tag{11}$$

at the bottom of the boundary. Equations (1)–(3) along with boundary conditions (4)–(11) can be solved if the length scales are specified.

The length scale Λ is obtained from[13]

$$\Lambda = 0{\cdot}25\{1{\cdot}8\,z_i[1-\exp(-4z/z_i)-0{\cdot}0003\,\exp(8z/z_i)]\} \tag{12}$$

for unstable stratification and from

$$\Lambda = \begin{cases} 0{\cdot}76\left(\dfrac{E}{(g/\theta)\mathrm{d}\theta/\mathrm{d}z}\right)^{1/2}, & \Lambda \leqslant \Delta z, \\ \Delta z, & \Lambda > \Delta z \end{cases} \tag{13}$$

for stable stratification, where z_i is the inversion height, z is the vertical height and Δz is the grid size in the vertical direction. The other length scales are specified as

$$\Lambda_2 = c_2 \Lambda, \tag{14}$$

$$\Lambda_3 = c_3 \Lambda. \tag{15}$$

The values of the constants $A = 0{\cdot}75$, $b = 0{\cdot}125$, $s = 1{\cdot}8$, $c_2 = 0{\cdot}3$ and $c_3 = -0{\cdot}3$ are based on Lewellen and Teske's second-order closure model.[10]

A TIME-SPLITTING FINITE ELEMENT SCHEME

As a result of extensive tests of different numerical schemes on the advective transport equation in air pollution modelling, Chock[16] concluded that the finite element method with linear basis function retains the peak value well, has tolerable spurious oscillations and requires short execution time and minimal memory storage. Currently, the time-splitting finite element scheme is commonly used for long-range transport problems with the inclusion of extensive atmospheric chemical reactions.[17] For these reasons we propose a time-splitting finite element scheme for the numerical solution of equations (1)–(3).

The domain was discretized into 96 grid points in the x=direction uniformly distributed with $\Delta x = 50$ m and 49 grid points in the vertical z-direction with $\Delta z = 25$ m for $z \leqslant z_i$ and $\Delta z = 50$ m for $z > z_i$. The governing equations of interest are lumped together into four groups owing to the similarity in the terms:

$$\begin{cases} \dfrac{\partial C_y}{\partial t} + U\dfrac{\partial C_y}{\partial x} = 0, & (16) \\ \dfrac{\partial \overline{wc_y}}{\partial t} + U\dfrac{\partial \overline{wc_y}}{\partial x} = 0, & (17) \\ \dfrac{\partial \overline{c\theta_y}}{\partial t} + U\dfrac{\partial \overline{c\theta_y}}{\partial x} + \dfrac{1}{3}\left(\dfrac{2bsq}{\Lambda}\right)\overline{c\theta_y} = 0; & (18) \end{cases}$$

$$\frac{\partial \overline{wc_y}}{\partial t} + \frac{1}{3}\left(\frac{Aq}{\Lambda}\right)\overline{wc_y} + \overline{uw}\frac{\partial C_y}{\partial x} - \frac{1}{3}\left(\frac{g}{\Theta}\right)\overline{c\theta_y} = 0; \tag{19}$$

$$\begin{cases} \dfrac{\partial C_y}{\partial t} + \dfrac{\partial \overline{wc_y}}{\partial z} = 0, & (20) \\ \dfrac{\partial \overline{wc_y}}{\partial t} + \dfrac{1}{3}\left(\dfrac{Aq}{\Lambda}\right)\overline{wc_y} + \overline{ww}\dfrac{\partial C_y}{\partial z} - \dfrac{1}{3}\left(\dfrac{g}{\Theta}\right)\overline{c\theta_y} = 0, & (21) \\ \dfrac{\partial \overline{c\theta_y}}{\partial t} + \dfrac{1}{3}\left(\dfrac{2bsq}{\Lambda}\right)\overline{c\theta_y} + \overline{w\theta}\dfrac{\partial C_y}{\partial z} + \dfrac{1}{2}\left(\dfrac{\mathrm{d}\Theta}{\mathrm{d}z}\right)\overline{wc_y} = 0; & (22) \end{cases}$$

$$\begin{cases} \dfrac{\partial \overline{wc_y}}{\partial t} + \dfrac{1}{3}\left(\dfrac{Aq}{\Lambda}\right)\overline{wc_y} - \dfrac{\partial}{\partial z}\left(\Lambda_2 q \dfrac{\partial \overline{wc_y}}{\partial z}\right) - \dfrac{1}{3}\left(\dfrac{g}{\Theta}\right)\overline{c\theta_y} = 0, & (23) \\ \dfrac{\partial \overline{c\theta_y}}{\partial t} + \dfrac{1}{3}\left(\dfrac{2bsq}{\Lambda}\right)\overline{c\theta_y} - \dfrac{\partial}{\partial z}\left(\Lambda_2 q \dfrac{\partial \overline{c\theta_y}}{\partial z}\right) + \dfrac{1}{2}\left(\dfrac{\mathrm{d}\Theta}{\mathrm{d}z}\right)\overline{wc_y} = 0. & (24) \end{cases}$$

Equations (16)–(19) are the governing transport equations for C_y, $\overline{wc_y}$ and $\overline{c\theta_y}$ in the x-direction. Equations (20)–(24) are the transport equations in the z-direction. Equations (16)–(22) were solved sequentially whereas equations (23) and (24) were solved simultaneously.

The finite element spatial discretization of (16)–(24) is performed using the Galerkin finite element method (GFEM) via the following expansions in the piecewise polynomial basis functions:

$$C_y(x,t) = \sum_{i=1}^{N} C_i(t)\, N_i(x), \qquad C_y(z,t) = \sum_{j=1}^{M} C_j(t)\, N_j(z), \tag{25a}$$

$$\overline{wc_y}(x,t) = \sum_{i=1}^{N} \overline{wc_i}(t)\, N_i(x), \qquad \overline{wc_y}(z,t) = \sum_{j=1}^{M} \overline{wc_j}(t)\, N_j(z), \tag{25b}$$

$$\overline{c\theta_y}(x,t) = \sum_{i=1}^{N} \overline{c\theta_i}(t)\, N_i(x), \qquad \overline{c\theta_y}(z,t) = \sum_{j=1}^{M} \overline{c\theta_j}(t)\, N_j(z), \tag{25c}$$

In the discretized domain there are N nodes in the x-direction and M nodes in the z-direction. In equations (25) the summations on the left correspond to approximations in the x-direction whereas those on the right correspond to the approximations in the z-direction. $N_i(x)$ and $N_j(z)$ are piecewise linear basis functions in the x- and z-directions respectively. Inserting equation (25) into the weak (Galerkin) form of (16)–(24) leads to the standard GFEM equations written in matrix notation as

$$[\mathbf{K}]\{\mathbf{\Phi}\} + [\mathbf{M}]\left\{\frac{\mathrm{d}\mathbf{\Phi}}{\mathrm{d}t}\right\} = \{\mathbf{f}\}, \tag{26}$$

where $\mathbf{\Phi}$ is a global vector containing all the nodal values of C_y, $\overline{wc_y}$ and $\overline{c\theta_y}$. $\mathbf{M}$ is the mass matrix, $\mathbf{K}$ is the 'advection plus diffusion' matrix and $\mathbf{f}$ is a 'source term' vector. The form of the mass matrix $\mathbf{M}$, the 'advection plus diffusion' matrix $\mathbf{K}$ and the source term vector $\mathbf{f}$ depends on the equation under study. For example, in equations (16) and (17) $\mathbf{K}$ has purely advection terms and there is no contribution to $\mathbf{f}$. However, in equation (18) $\mathbf{K}$ will have contributions from the third term on the LHS as well. For equations (19), (21) and (22) $\mathbf{K}$ will have contributions only from the second term on the LHS and $\mathbf{f}$ has contributions from the third and fourth terms on the LHS. Since equations (16)–(22) are solved sequentially, the matrices $\mathbf{K}$ and $\mathbf{M}$ will be of the block tridiagonal type and $\mathbf{f}$ will incorporate the natural boundary conditions.

The semidiscretized equations are integrated in time using either the Crank–Nicolson (implicit) or the forward (explicit) Euler scheme, depending on the nature of the equations. Since equations (16)–(18) contain only the dependent variables C_y, $\overline{wc_y}$ and $\overline{c\theta_y}$ respectively, there is no contribution to the RHS of equation (26) (the $\mathbf{f}$-term) after spatial discretization. The Crank–Nicolson (implicit) scheme was used for the temporal discretization of equations (16)–(18). On the other hand, equations (19)–(22) contain terms other than the dependent variables and contribute to the $\mathbf{f}$-term in equation (26). Therefore the Euler scheme (explicit) was used for temporal discretization of equations (19)–(22). Equations (23) and (24) are coupled and the Crank–Nicolson (implicit) scheme was used for greater numerical stability.

Application of the Crank–Nicolson scheme to the standard GFEM equation (26) arising from equations (16)–(18) leads to

$$[\mathbf{K}]\left\{\frac{\Phi_i^{n+1}+\Phi_i^n}{2}\right\}+[\mathbf{M}]\left\{\frac{\Phi_i^{n+1}-\Phi_i^n}{\Delta t}\right\}=0. \tag{27}$$

Rearrangement of equation (27) gives

$$\left[\frac{\mathbf{M}}{\Delta t}+\frac{\mathbf{K}}{2}\right]\{\Phi_i^{n+1}\}=\left[\frac{\mathbf{M}}{\Delta t}-\frac{\mathbf{K}}{2}\right]\{\Phi_i^n\}, \tag{28}$$

where Φ_i^n are the discrete nodal values of the unknowns C_y, $\overline{wc_y}$ and $\overline{c\theta_y}$ at time step n and Φ_i^{n+1} are the discrete nodal values of the unknowns C_y, $\overline{wc_y}$ and $\overline{c\theta_y}$ at time step $n+1$.

Similarly, application of the forward Euler scheme to equation (26) arising from spatial discretization of equations (19)–(22) leads to

$$[\mathbf{K}]\{\Phi_i^n\}+[\mathbf{M}]\left\{\frac{\Phi_i^{n+1}-\Phi_i^n}{\Delta t}\right\}=\{\mathbf{f}\}. \tag{29}$$

Rearrangement of equation (29) gives

$$\left[\frac{\mathbf{M}}{\Delta t}\right]\{\Phi_i^{n+1}\}=\left[\frac{\mathbf{M}}{\Delta t}-\mathbf{K}\right]\{\Phi_i^n\}+\{\mathbf{f}\}. \tag{30}$$

It should be noted that equations (16)–(22) were solved individually and sequentially whereas equations (23) and (24) were solved simultaneously. Solution of equations (16)–(19) at each jth vertical grid point completes one sweep in the x-direction. This sweep gives the values of C_y, $\overline{wc_y}$ and $\overline{c\theta_y}$ at each grid point for some intermediate time step. Using these values, equations (20)–(24) are solved at each jth horizontal grid point, completing the sweep in the z-direction. This sweep gives the solution of C_y, $\overline{wc_y}$ and $\overline{c\theta_y}$ at the next time step. The time step must be chosen such that the Courant number criterion is satisfied. The boundary conditions in the x-direction according to equations (4) and (6) are used for every sweep in the x-direction. Natural boundary conditions are used at the rightmost boundary. The boundary conditions in the z-direction according to equations (10) and (11) are used for every sweep in the z-direction.

The details of the time-splitting technique are as follows:

$$\left[\frac{\mathbf{M}_x}{\Delta t}+\frac{\mathbf{K}_x^1}{2}\right]\{\mathbf{C}^*\}=\left[\frac{\mathbf{M}_x}{\Delta t}-\frac{\mathbf{K}_x^1}{2}\right]\{\mathbf{C}^n\}, \tag{31}$$

$$\left[\frac{\mathbf{M}_x}{\Delta t}+\frac{\mathbf{K}_x^1}{2}\right]\{\overline{wc}^*\}=\left[\frac{\mathbf{M}_x}{\Delta t}-\frac{\mathbf{K}_x^1}{2}\right]\{\overline{wc}^n\}, \tag{32}$$

$$\left[\frac{\mathbf{M}_x}{\Delta t}+\frac{\mathbf{K}_x^2}{2}\right]\{\overline{c\theta}^*\}=\left[\frac{\mathbf{M}_x}{\Delta t}-\frac{\mathbf{K}_x^2}{2}\right]\{\overline{c\theta}^*\}, \tag{33}$$

$$\left[\frac{\mathbf{M}_x}{\Delta t}\right]\{\overline{wc}^{**}\}=\{\mathbf{f}_x\}+\left[\frac{\mathbf{M}_x}{\Delta t}-\mathbf{K}_x^3\right]\{\overline{wc}^*\}, \tag{34}$$

$$\left[\frac{\mathbf{M}_z}{\Delta t}\right]\{\mathbf{C}^{n+1}\}=\{\mathbf{f}_z^1\}+\left[\frac{\mathbf{M}_z}{\Delta t}\right]\{\mathbf{C}^*\}, \tag{35}$$

$$\left[\frac{\mathbf{M}_z}{\Delta t}\right]\{\overline{wc}^{***}\}=\{\mathbf{f}_z^2\}+\left[\frac{\mathbf{M}_z}{\Delta t}-\mathbf{K}_z^1\right]\{\overline{wc}^{**}\}, \tag{36}$$

$$\left[\frac{\mathbf{M}_z}{\Delta t}\right]\{\overline{c\theta}^{**}\} = \{\mathbf{f}_x^3\} + \left[\frac{\mathbf{M}_z}{\Delta t} - \mathbf{K}_z^2\right]\{\overline{c\theta}^{*}\}, \tag{37}$$

$$\left[\frac{\mathbf{M}_z}{\Delta t} + \frac{\mathbf{K}_z^3}{2}\right]\{\overline{wc}^{n+1}\} + \left[\frac{\mathbf{K}_z^4}{2}\right]\{\overline{c\theta}^{n+1}\} = \{\mathbf{f}_z^4\} + \left[\frac{\mathbf{M}_z}{\Delta t} - \frac{\mathbf{K}_z^3}{2}\right]\{\overline{wc}^{***}\} - \left[\frac{\mathbf{K}_z^4}{2}\right]\{\overline{c\theta}^{**}\}, \tag{38}$$

$$\left[\frac{\mathbf{K}_z^5}{2}\right]\{\overline{wc}^{n+1}\} + \left[\frac{\mathbf{M}_z}{\Delta t} + \frac{\mathbf{K}_z^6}{2}\right]\{\overline{c\theta}^{n+1}\} = \{\mathbf{f}_z^5\} - \left[\frac{\mathbf{K}_z^5}{2}\right]\{\overline{wc}^{***}\} + \left[\frac{\mathbf{M}_z}{\Delta t} - \frac{\mathbf{K}_z^6}{2}\right]\{\overline{c\theta}^{**}\}. \tag{39}$$

The subscript and superscript notation for the mass matrix, advection matrix and source term vector have been used to differentiate the individual matrices arising from the Galerkin scheme of equations (16)–(18). Thus $\mathbf{M}_x$ is the mass matrix from equations (16)–(18) and the subscript x denotes the x-direction transport equations. Similarly, $\mathbf{K}_x^1$, $\mathbf{K}_x^2$ and $\mathbf{K}_x^3$ are the advection matrices from the x-direction equations (16)–(19) and $\mathbf{f}_x$ is the source term vector for the x-direction in equation (19). Subscript z is used for the z-direction transport equations (20)–(24).

EDDY DIFFUSIVITY MODEL

Although it is well known that the first-order closure turbulence model (eddy diffusivity or K-diffusion model) cannot describe the plume behaviour in convective boundary layers,[7–15] it

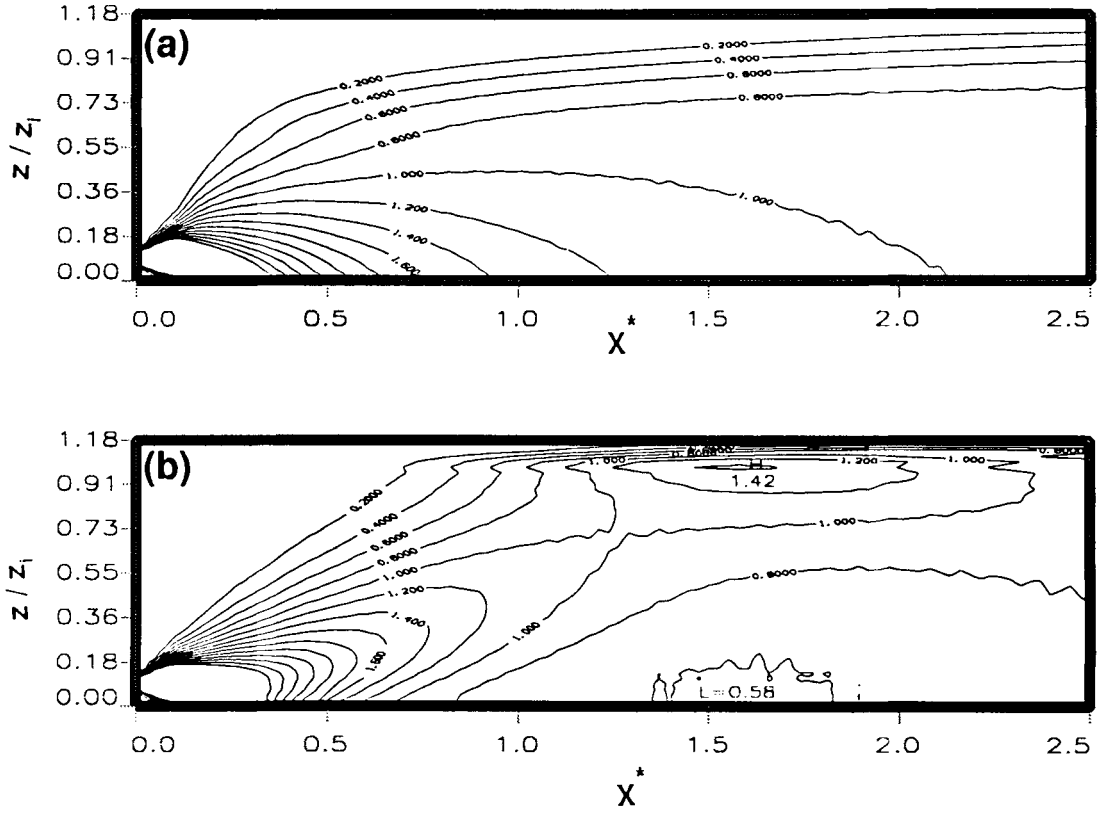

Figure 1. Steady state contours of the non-dimensional cross-wind integrated concentration as a function of dimensionless height and dimensionless downwind distance calculated from (a) the K-diffusion model and (b) the second-order closure model. The source is at $z_s/z_i = 0{\cdot}09$ (100 m)

remains the most popular model in air pollution studies. So far these studies have not explicitly compared the plume behaviour predicted by the K-diffusion model with that predicted by LES or other second-order closure models.

The K-diffusion model in its two-dimensional form[18] is given by

$$\frac{\partial C_y}{\partial t}+U\frac{\partial C_y}{\partial x}=\frac{\partial}{\partial z}\left(K_{zz}\frac{\partial C_y}{\partial z}\right), \tag{40}$$

where $K_{zz}(z)$ is the eddy diffusivity determined from the empirical expression of Lamb and Duran.[19] It is based on the Monin–Obukhov similarity theory coupled with observational or computationally generated data.

In order to compare the K-diffusion theory with the second-order closure model, a time-splitting finite element scheme similar to the one described previously is used to solve equation (40) for the same source strength and wind profile $U(z)$ with the same grid system and time step.

RESULTS AND DISCUSSION

Using the turbulence variables calculated from a modified Mellor–Yamada level 3 model,[20] Enger[12] showed that the second-order closure model agreed qualitatively with Willis and Deardorff's experiments.[1–4] Sun[13] used a simple one-dimensional model to calculate mean flow quantities and the turbulence variables and improved upon Enger's results. More recently,

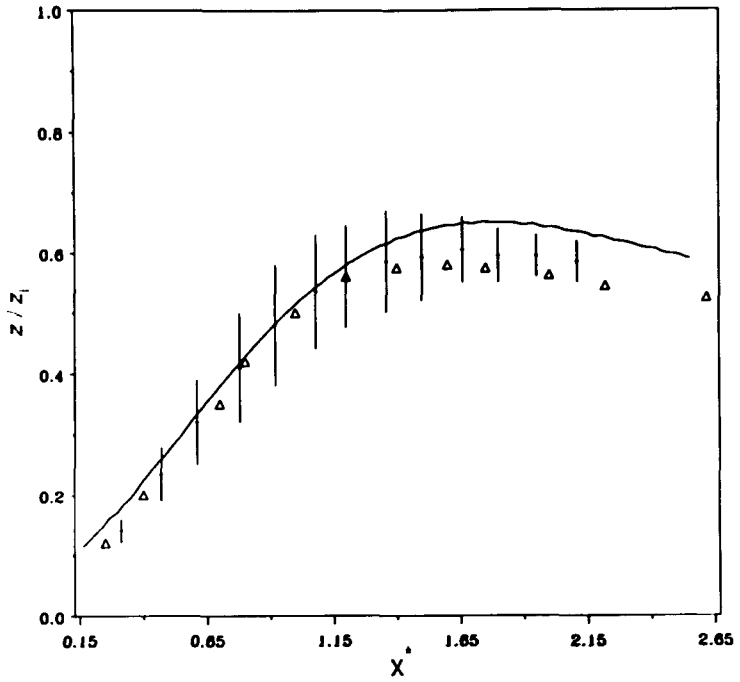

Figure 2. The mean plume height non-dimensionalized with inversion height z_i as a function of dimensionless downwind distance. The solid line is the second-order closure model result. The triangles are from Willis and Deardorff's tank experiment[2] for $z_s/z_i = 0{\cdot}067$. The vertical bars indicate the standard deviation over six large-eddy simulation experiments[9]

Nieuwstadt and De Valk[9] used a large-eddy model to simulate buoyant and non-buoyant plume behaviour. These studies use finite difference schemes to simulate the dispersion of passive contaminants from near-ground and elevated sources.

In order to compare the results of the present model with some of the previous studies, we introduce the following dimensionless parameters:

$$C_y^* = (U_m z_i / Q) C_y, \tag{41}$$

$$\overline{wc_y}^* = (U_m z_i / Q w_*) \overline{wc_y}, \tag{42}$$

$$\overline{c\theta_y}^* = (U_m z_i / Q \theta_*) \overline{c\theta_y}, \tag{43}$$

$$X^* = (w_* / z_i U_m) x, \tag{44}$$

$$Z^* = z / z_i, \tag{45}$$

where C_y^*, $\overline{wc_y}^*$ and $\overline{c\theta_y}^*$ are the dimensionless cross-wind integrated concentration, concentration flux and covariance of concentration and temperature respectively. X^* is the dimensionless downwind distance and Z^* is the dimensionless vertical height. U_m is the mean wind speed in the

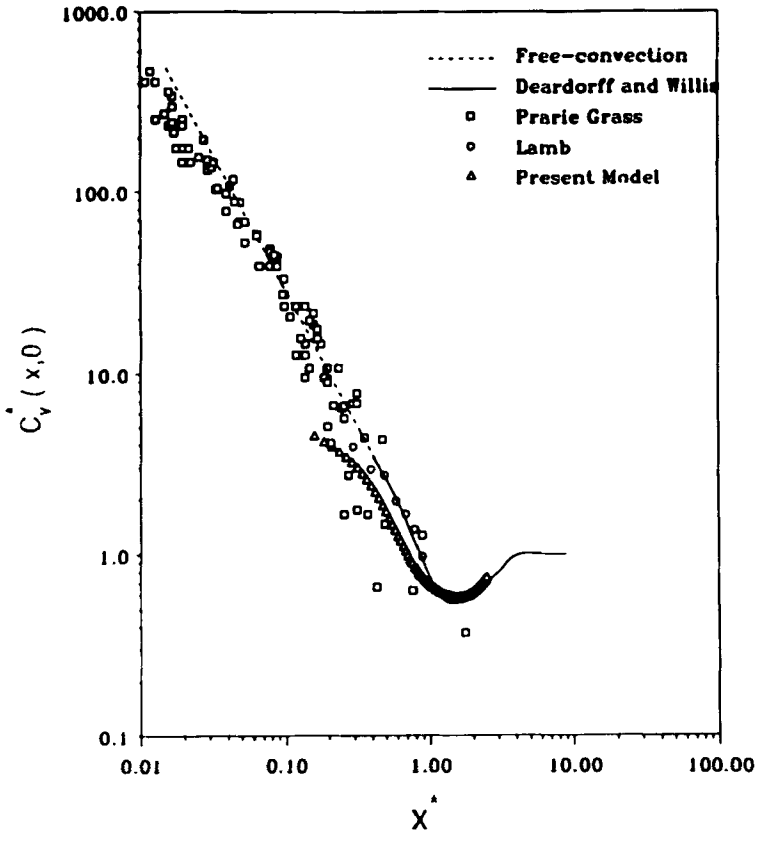

Figure 3. Comparison of the calculated non-dimensional cross-wind integrated concentration at ground level as a function of dimensionless downwind distance with Prairie Grass data,[21] free-convection similarity theory,[21] Lamb's results[22] and Willis and Deardorff's data[1]

convective boundary layer, w_* is the convective velocity scale, θ_* is the convective temperature scale, z_i is the inversion height and Q is the source strength. The following simulations are carried out for 14:00 EST during day 33 of the Wangara experiments. The ratio U_m/w_* is about 1·69.

Case A 'Near-ground-level source': $z_s/z_i = 0{\cdot}09$ (100 m)

Figure 1(a) shows the plume behaviour for a near-ground emission simulated by the K-diffusion model (equation (40)), whereas Figure 1(b) shows that the second-order turbulence closure model in the present work can simulate the plume 'lift-off' phenomenon and predict a local maximum of $C_y^* = 1{\cdot}42$ at a downwind distance of $X^* = 1{\cdot}56$ and a vertical height of $Z^* = 0{\cdot}98$. This 'lift-off' phenomenon has been confirmed recently by Poreh and Cermak's wind-tunnel experiment.[5] The downwind location of this maximum compares well with the LES results of Nieuwstadt and De Valk[9] and with Deardorff and Willis's laboratory data.[1,2] However, the local maximum is reached at a vertical height of $Z^* = 0{\cdot}98$ in contrast to the LES results where $Z^* = 0{\cdot}8$. This could be due to the difference in the treatment of boundary conditions at the top of the boundary layer. In the present model we adopted Sun's approach[13] and consider an overlying stable boundary layer above inversion which permits the diffusion process. Thus the vertical location of the local maximum in this work agrees with that of Sun's work. Figure 2 shows that the mean plume height calculated by the present model compares favourably with the LES results and the experimental data.[2] Figure 3 compares the ground-level cross-wind integrated concentration between the Prairie Grass field data,[21] the $\frac{3}{2}$ power law from free-convection theory,[21]

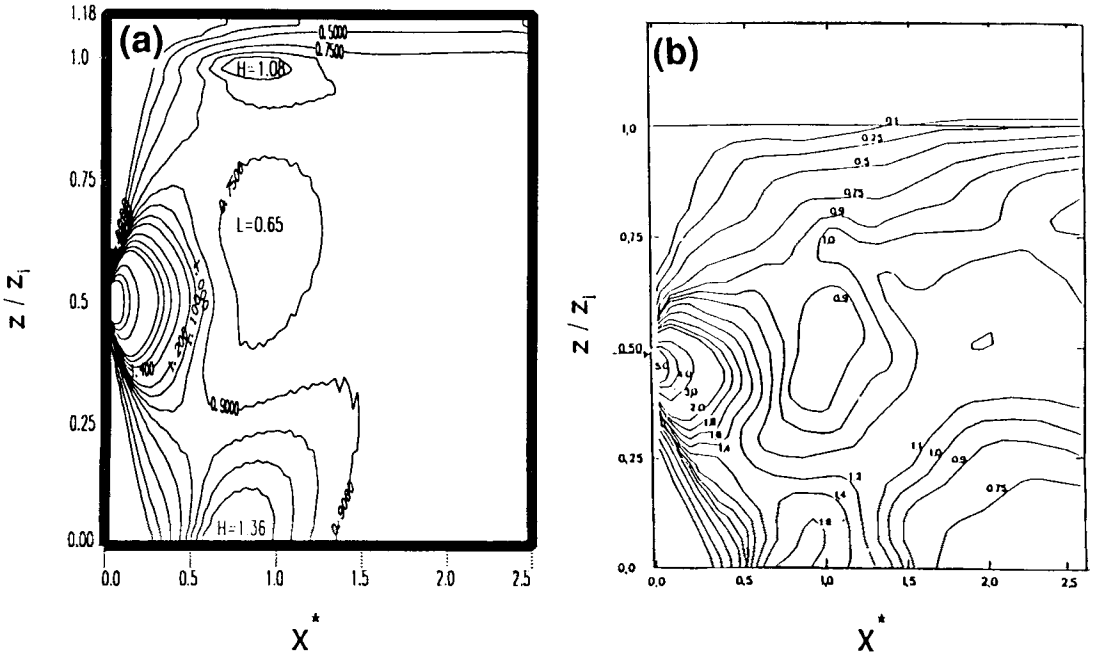

Figure 4. Steady state contours of the non-dimensional cross-wind integrated concentration as a function of dimensionless height and dimensionless distance calculated from (a) the second-order closure model with the source at $z_s/z_i = 0{\cdot}50$ (550 m) (the grid size for this simulation was $\Delta z = 25$ m, $\Delta x = 50$ m) and (b) the large-eddy model[9] ($z_s/z_i = 0{\cdot}49$)

Lamb's numerical results[22] ($z_s/z_i = 0{\cdot}025$), Deardorff and Willis's experiments[1] ($z_s/z_i = 0{\cdot}067$, concentration measured at $z/z_i = 0{\cdot}05$) and the second-order closure model of this work.

Case B. 'Source in the middle of the mixed layer': $z_s/z_i = 0{\cdot}5$ (550 m)

Figure 4(a) shows the contours of C_y^* for the release of the passive material in the middle of the mixed layer predicted by our model. Figure 4(b) shows the numerical results of the LES model of Nieuwstadt and De Valk. Our model results show that the plume centreline descends and impinges on the ground with a value of $C_y^* = 1{\cdot}36$ at $X^* = 0{\cdot}73$, which agrees well with Willis and Deardorff's experiments[4] ($C_y^* = 1{\cdot}8$, $X^* = 0{\cdot}8$). Our results give a local minimum at $X^* = 0{\cdot}89$ and $Z^* = 0{\cdot}63$ which agrees with the LES result, whereas Enger's results do not clearly show this minimum. There is also an elevated maximum with a value of $C_y^* = 1{\cdot}08$ at $X^* = 0{\cdot}91$ and $Z^* = 0{\cdot}98$. In order to ascertain the existence of this elevated local maximum, we have carried out simulation using different vertical grid sizes. The horizontal grid size remains the same at 50 m. Results for a vertical grid size of 20 m and for a coarser grid of 50 m both have the same features as those shown in Figure 4(a). Furthermore, the mass conservation, which is a measure of accuracy for various numerical schemes, is about 98·6% for Figure 4(a).

The choice of model parameters and the calculations of turbulence variables are critical issues in higher-order closure modelling of turbulent flows. Therefore it is important to see the effects of

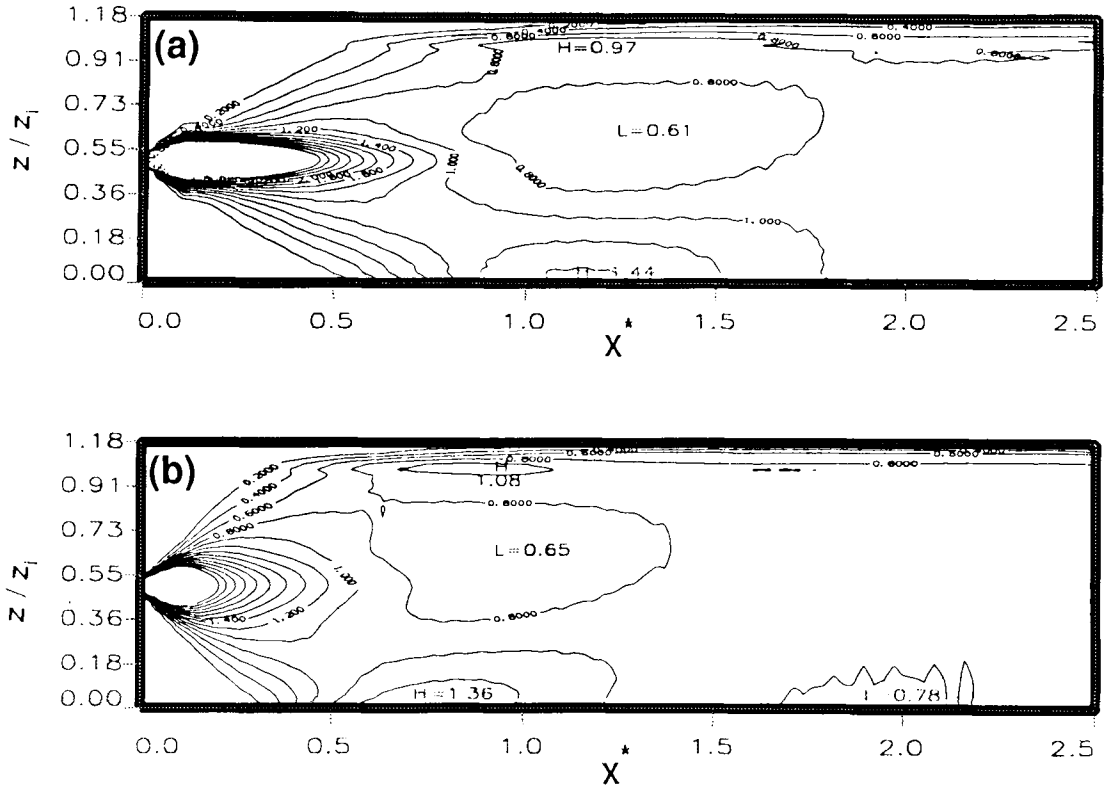

Figure 5. Steady state contours of the non-dimensional cross-wind integrated concentration as a function of dimensionless height and dimensionless downwind distance calculated from (a) Sun's model parameters and turbulence variables and (b) the second-order closure model in this work with the source at $z_s/z_i = 0{\cdot}50$ (550 m)

model parameters and turbulence variables on the concentration contours. Figure 5 compares the results calculated from Sun's model parameters and turbulence variables with those calculated from this work. Sun's model predicted an elevated local maximum of $C_y^* = 0{\cdot}97$ at $X^* = 1{\cdot}15$ and $Z^* = 0{\cdot}97$. The differences in downwind location of the local maxima and minimum between Sun's model and the present model are probably due to the differences in the vertical profiles of the turbulence variables. Figure 6 compares the K-diffusion theory and the second-order model. It is clear that the K-diffusion theory does not provide the local maxima and minimum which are predicted by the LES and second-order closure models.

The CPU times used by the second-order closure model are about 18 times used by the K-diffusion model because there are two additional partial differential equations for the second-order closure model. Furthermore, equations (1)–(3) are much more complicated than equation (40). There are nine time-split equations with source terms for the second-order closure model (Equations (16)–(24)) whereas there are only two simple time-split equations for the K-diffusion model. For the grid system of $\Delta x = 50$ m and $\Delta z = 25$ m with $\Delta t = 1$ s, the CPU times are 1517 and 84 s for the second-order closure model and the K-diffusion theory respectively. For $\Delta x = 100$ m, $\Delta z = 50$ m and $\Delta t = 2$ s, the CPU times decrease to 208 and 13 s respectively on an IBM 3090-300E machine. Even with these coarse grids, the second-order closure model provides accurate information on the local maxima and minimum, with values close to those in Figure 6(b).

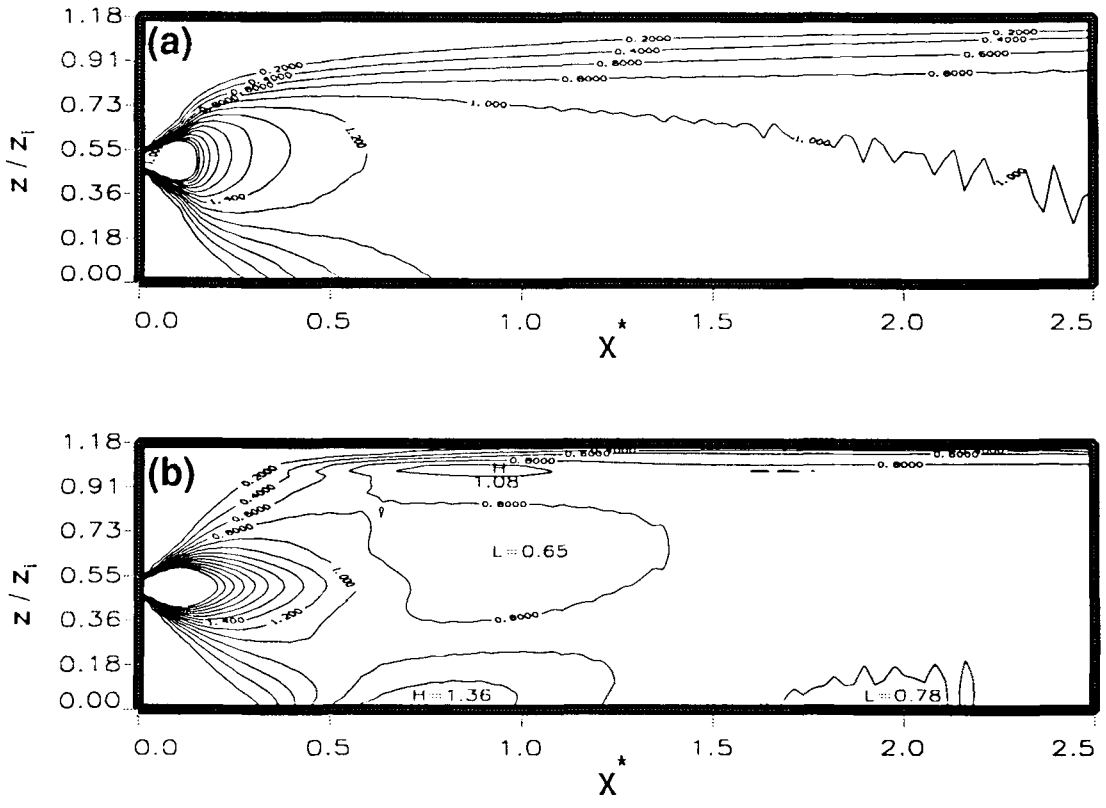

Figure 6. Steady state contours of the non-dimensional cross-wind integrated concentration as a function of dimensionless height and dimensionless downwind distance calculated from (a) the K-diffusion model and (b) the second-order closure model with the source at $z_s/z_i = 0{\cdot}50$ (550 m)

However, the spurious oscillations in Figure 6(a) become intolerable for the K-diffusion theory. Since equations (16)–(24) derived by the time-splitting scheme can be solved in parallel, we expect that parallelization of the code will make the algorithm even more computationally efficient.

CONCLUSIONS

It is demonstrated that the second-order closure model can simulate the correct plume behaviour in a convective boundary layer. The model results compare well with large-eddy simulations, laboratory data and field tests, whereas the commonly used K-diffusion model cannot describe the plume behaviour in convective boundary layers. Furthermore, it is shown that the model parameters and turbulence variables have effects on the plume behaviour with regard to the location of local maximum and minimum concentrations.

ACKNOWLEDGEMENTS

This work is partially supported by the Center for Computational Sciences at the University of Kentucky and the U.S. Army Chemical Research and Development Engineering Center.

APPENDIX

Here our objective is to use a second-order closure model to calculate the vertical profiles of the mean and turbulence variables which must be provided in equations (1)–(3). The mean field equations for a horizontally homogeneous flow whose properties depend only on height z and time t are

$$\frac{\partial U}{\partial t}=fV-fV_g-\frac{\partial(\overline{uw})}{\partial z}, \tag{46}$$

$$\frac{\partial V}{\partial t}=-fU+fU_g-\frac{\partial(\overline{vw})}{\partial z}, \tag{47}$$

$$\frac{\partial \Theta}{\partial t}=-\frac{\partial(\overline{w\theta})}{\partial z}, \tag{48}$$

where U and V are the mean horizontal wind velocities, Θ is the mean temperature and $f=-0{\cdot}826\times10^{-4}\ \mathrm{s}^{-1}$ is the Coriolis parameter at Hay, Australia (34°30′S, 144°56′E). U_g and V_g are the components of the geostrophic wind.

An invariant second-order closure model of turbulent shear flow developed by Lewellen and Teske[10] and Donaldson[11] for the atmospheric surface layer is extended to a convective boundary layer. With the assumption of horizontal homogeneity, the one-dimensional unsteady state differential equations for determining the turbulence variables from the second-order closure model are

$$\frac{\partial\overline{uu}}{\partial t}=-2\overline{uw}\frac{\partial U}{\partial z}+\frac{\partial}{\partial z}\left(\Lambda_2 q\frac{\partial}{\partial z}(\overline{uu})\right)-\frac{q}{\Lambda}\left(\overline{uu}-\frac{q^2}{3}\right)-\frac{2bq^3}{3\Lambda}, \tag{49}$$

$$\frac{\partial\overline{vv}}{\partial t}=-2\overline{vw}\frac{\partial V}{\partial z}+\frac{\partial}{\partial z}\left(\Lambda_2 q\frac{\partial}{\partial z}(\overline{vv})\right)-\frac{q}{\Lambda}\left(\overline{vv}-\frac{q^2}{3}\right)-\frac{2bq^3}{3\Lambda}, \tag{50}$$

$$\frac{\partial \overline{ww}}{\partial t} = \frac{2g}{\Theta_0}\overline{w\theta} + 3\frac{\partial}{\partial z}\left(\Lambda_2 q \frac{\partial}{\partial z}(\overline{ww})\right) + 2\frac{\partial}{\partial z}\left(\Lambda_3 q \frac{\partial}{\partial z}(\overline{ww})\right) - \frac{q}{\Lambda}\left(\overline{ww} - \frac{q^2}{3}\right) - \frac{2bq^3}{3\Lambda}, \tag{51}$$

$$\frac{\partial \overline{uw}}{\partial t} = -\overline{ww}\frac{dU}{dz} + \frac{g}{\Theta_0}\overline{u\theta} + 2\frac{\partial}{\partial z}\left(\Lambda_2 q \frac{\partial}{\partial z}(\overline{uw})\right) + \frac{\partial}{\partial z}\left(\Lambda_3 q \frac{\partial}{\partial z}(\overline{uw})\right) - \frac{q\overline{uw}}{\Lambda}, \tag{52}$$

$$\frac{\partial \overline{vw}}{\partial t} = -\overline{ww}\frac{\partial V}{\partial z} + \frac{g}{\Theta_0}\overline{v\theta} + 2\frac{\partial}{\partial z}\left(\Lambda_2 q \frac{\partial}{\partial z}(\overline{vw})\right) + \frac{\partial}{\partial z}\left(\Lambda_3 q \frac{\partial}{\partial z}(\overline{vw})\right) - \frac{q\overline{vw}}{\Lambda}, \tag{53}$$

$$\frac{\partial \overline{u\theta}}{\partial t} = -\overline{uw}\frac{\partial \Theta}{\partial z} - \overline{w\theta}\frac{\partial U}{\partial z} + \frac{\partial}{\partial z}\left(\Lambda_2 q \frac{\partial}{\partial z}(\overline{u\theta})\right) - \frac{Aq\overline{u\theta}}{\Lambda}, \tag{54}$$

$$\frac{\partial \overline{v\theta}}{\partial t} = -\overline{vw}\frac{\partial \Theta}{\partial z} - \overline{w\theta}\frac{\partial V}{\partial z} + \frac{\partial}{\partial z}\left(\Lambda_2 q \frac{\partial}{\partial z}(\overline{v\theta})\right) - \frac{Aq\overline{v\theta}}{\Lambda}, \tag{55}$$

$$\frac{\partial \overline{w\theta}}{\partial t} = -\overline{ww}\frac{\partial \Theta}{\partial z} + \frac{g}{\Theta_0}\overline{\theta^2} + 2\frac{\partial}{\partial z}\left(\Lambda_2 q \frac{\partial}{\partial z}(\overline{w\theta})\right) + \frac{\partial}{\partial z}\left(\Lambda_3 q \frac{\partial}{\partial z}(\overline{w\theta})\right) - \frac{Aq\overline{w\theta}}{\Lambda}, \tag{56}$$

$$\frac{\partial \overline{\theta^2}}{\partial t} = -2\overline{w\theta}\frac{\partial \Theta}{\partial z} + \frac{\partial}{\partial z}\left(\Lambda_2 q \frac{\partial}{\partial z}(\overline{\theta^2})\right) - \frac{2bsq\overline{\theta^2}}{\Lambda}, \tag{57}$$

where $\overline{uu}$, $\overline{vv}$, $\overline{ww}$, $\overline{uw}$ and $\overline{vw}$ are the components of the Reynolds stress tensor. The equation for $\overline{uv}$ is not included because $\overline{uv}$ does not appear in other Reynolds stress equations. $\overline{u\theta}$, $\overline{v\theta}$ and $\overline{w\theta}$ are the components of the turbulent heat flux; $\overline{\theta^2}$ is the temperature variance. These equations represent a balance between production, transport and destruction processes for the Reynolds stress equations, temperature flux equations and temperature variance equation. Terms with length scales Λ_2 and Λ_3 represent parametrizations of the velocity diffusion term and the pressure diffusion term respectively. Equations (46)–(57) form a set of equations for the mean and turbulence variables.

Since $\overline{uu}$ and $\overline{vv}$ appear in other equations only in terms of q, equations (49)–(51) can be combined to form one equation for the turbulent velocity q ($=\overline{u_i u_i}^{1/2}$):

$$\frac{\partial \bar{q}^2}{\partial t} = -2\overline{uw}\frac{dU}{dz} - 2\overline{vw}\frac{dV}{dz} + 2\frac{g}{\Theta_0}\overline{w\theta} + \frac{d}{dz}\left(\Lambda_2 q \frac{d}{dz}q^2\right) + 2\frac{d}{dz}\left(\Lambda_2 q \frac{d}{dz}(\overline{ww})\right) + 2\frac{d}{dz}\left(\Lambda_3 q \frac{d}{dz}(\overline{ww})\right) - \frac{2bq^3}{\Lambda}. \tag{58}$$

Equations (46)–(48) and (51)–(58) form a set of 11 partial differential equations with three unknown mean variables, U, V and Θ, and eight unknown turbulent variables, q, $\overline{ww}$, $\overline{uw}$, $\overline{vw}$, $\overline{u\theta}$, $\overline{v\theta}$, $\overline{w\theta}$ and $\overline{\theta^2}$. The length scales appearing in the above equations are given by equations (12)–(15), thus giving a closed set 11 time-dependent partial differential equations to determine the mean and turbulence variables. The above set of equations were solved numerically using SPRINT,[23] which is a general-purpose computer program for the numerical solution of mathematical models that involve mixed systems of time-dependent algebraic, ordinary and partial differential equations. The partial differential equations are solved by using a method-of-lines approach in which the problem is discretized in space and then integrated in time. The grids in the vertical direction are evenly spaced, with the uppermost grid point at 2·0 km. Since we were interested in the 14:00 EST profiles, the initial profiles for 12:00 EST were specified for the mean

and turbulence variables. The lower boundary conditions are consistent with the Monin–Obukhov similarity.[24] The mean gradients and turbulence quantities were set to zero at the upper boundary.

Figure 7 compares our model prediction with other models[15] for the dimensionless turbulent kinetic energy ($E/w_*^2 = \frac{1}{2}q^2/w_*^2$). It should be noted that in Figure 7, except for Willis and Deardorff's experimental data,[25] all the vertical profiles are generated by one-dimensional models. The model by André *et al.*[26] is the most sophisticated and contains 34 differential equations for the turbulence variables because it is a third-order closure model. Enger[12] modified and used Mellor and Yamada's level 3 model,[20], which requires equations for turbulent kinetic energy and temperature variance. Sun and Chang's simplified model[15] uses mean flow equations with first-order closures and an equation for turbulent kinetic energy. Therefore it cannot simulate the temperature variance. For the sake of brevity, it suffices to say that our model predictions for other turbulence variables compare well with the results of Deardorff[27] (LES), Wyngaard and Cote[28] (second-order closure model with a transport equation for dissipation) and Sun and Ogura[29] (modified Mellor–Yamada level 3 model). The CPU times for the numerical solution of equations (46)–(48) and (51)–(58) are 1625, 985 and 409 s for 81, 61 and 41 grid points respectively. The numerical solutions using 41 grid points show slight oscillations

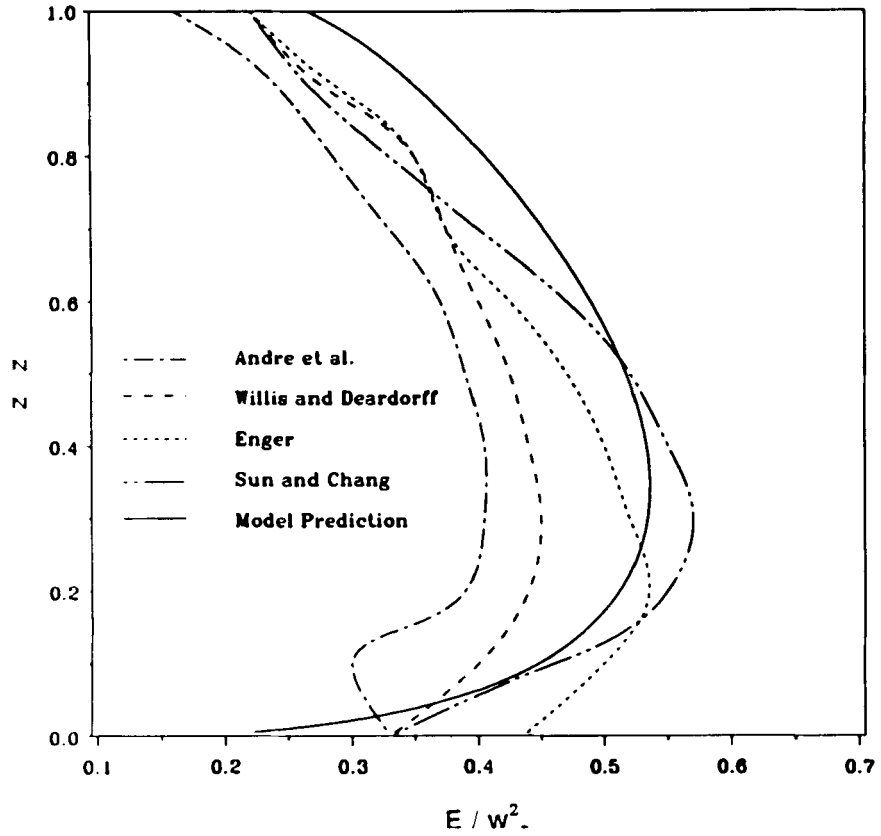

Figure 7. Comparison of our model prediction (solid line) with other vertical profiles of normalized turbulent kinetic energy (Andre *et al.*,[26] Willis and Deardorff,[25] Enger[12] and Sun and Chang[15])

within the first 400 m from the ground. However, the profiles are quite close to those obtained with 81 grid points.

REFERENCES

1. J. W. Deardorff and G. E. Willis, 'A parameterization of diffusion into the mixed layer', *J. Appl. Meteorol.*, **14,** 1451–1458 (1975).
2. G. E. Willis and J. W. Deardorff, 'A laboratory model of diffusion into the convective planetary boundary layer', *Q. J. R. Meteorol. Soc.*, **102,** 427–445 (1976).
3. G. E. Willis and J. W. Deardorff, 'A laboratory study of dispersion from an elevated source within a modeled convective planetary boundary layer', *Atmos. Environ.* **12,** 1305–1311 (1978).
4. G. E. Willis and J. W. Deardorff, 'A laboratory study of dispersion from a source in the middle of the convective mixed layer', *Atmos. Environ.* **15,** 109–117 (1981).
5. M. Poreh and J. E. Cermak, 'Diffusion in an atmospheric layer with an elevated inversion', in R. H. Kohl (ed.), *Proc. 1985 Scientific Conf. on Obscuration and Aerosol Research*, U.S. Army Chemical Research and Development Engineering Center, Aberdeen Proving Ground, 1986, pp. 113–115.
6. W. R. Moninger, W. L. Eberhard, G. A. Briggs, R. A. Kropfli and J. C. Kaimal, 'Simultaneous radar and lidar observations of plumes from continuous point sources', *Preprints, 21st Radar Meteorology Conf.*, American Meteorological Society, Boston, 1983, pp. 246–250.
7. J. W. Deardorff, 'Numerical investigation of neutral and unstable planetary boundary layer', *J. Atmos. Sci.*, **29,** 91–115 (1972).
8. C. H. Moeng, 'A large eddy simulation model for the study of planetary boundary layer turbulence', *J. Atmos. Sci.*, **41,** 2052–2062 (1984).
9. F. T. M. Nieuwstadt and J. P. J. M. M. De Valk, 'A large eddy simulation of buoyant and non-buoyant plume dispersion in the atmospheric boundary layer', *Atmos. Environ.*, **21,** 2573–2587 (1987).
10. W. S. Lewellen and M. Teske, 'Prediction of the Monin–Obukhov similarity functions from an invariant model of turbulence', *J. Atmos. Sci.*, **30,** 1340–1345 (1973).
11. C. duP. Donaldson, 'Construction of a dynamic model of production of atmospheric turbulence and the dispersal of atmospheric pollutants', in P. A. Haugen (ed.), *Workshop of Micrometeorology*, American Meteorological society, Boston, 1973, pp. 313–392.
12. L. Enger, 'A higher order closure model applied to dispersion in a convective PBL', *Atmos. Environ.*, **20,** 879–894 (1986).
13. W.-Y. Sun, 'Air pollution in a convective boundary layer', *Atmos. Environ.*, **20,** 1877–1886 (1986).
14. J. W. Deardorff, 'Stratocumulus-capped mixed layers derived from a three-dimensional model', *Boundary Layer Meteorol.*, **18,** 495–527 (1980).
15. W.-Y. Sun and C.-Z. Chang, 'Diffusion model for a convective layer. Part I: Numerical simulation of convective boundary layer', *J. Climate Appl. Meteorol.*, **25,** 1445–1453 (1986).
16. D. P. Chock, 'A comparison of numerical methods for solving the advection equation—II', *Atmos. Environ.*, **19,** 571–586 (1985).
17. G. R. Carmichael, L. K. Peters and T. Kitada, 'A second generation model for regional-scale transport/chemistry/deposition.', *Atmos. Environ.*, **20,** 173–188 (1986).
18. T. H. Tsang, R. Solis and J. R. Brock, 'Comparison of calculated and observed super and sub-micrometer aerosol mass concentrations using St. Louis RAPS data base', *Atmos. Environ.*, **17,** 1291–1298 (1983).
19. R. G. Lamb and D. R. Duran, 'Eddy diffusivities derived from a numerical model of the convective boundary layer', *Nuovo Cimento*, **1C,** 1–17 (1977).
20. G. L. Mellor and T. Yamada, 'A hierarchy of turbulence closure models for planetary boundary layers', *J. Atmos. Sci.*, **31,** 1791–1806 (1974).
21. F. T. M. Nieuwstadt, 'Application of mixed-layer similarity to the observed dispersion from a ground level source', *J. Appl. Meteorol.*, **19,** 157–162 (1980).
22. R. G. Lamb, 'The effects of release height on material dispersion in the convective boundary layer', *Preprint Vol., AMS Fourth Symp. on Turbulence, Diffusion and Air Pollution*, American Meteorological Society, 1979, pp. 27–33.
23. M. Berzins and R. M. Furzeland, 'A user's manual for SPRINT—a versatile software package for solving systems of algebraic, ordinary and partial differential equatons: Parts 1 & 2', Thornton Research Centre, Shell Research Limited, Amsterdam 1985.
24. J. A. Businger, J. C. Wyngaard, Y. Izumi and E. F. Bradley, 'Flux-profile relationships in the atmospheric surface layer', *J. Atmos. Sci.*, **28,** 181–189 (1971).
25. G. E. Willis and J. W. Deardorff, 'A laboratory model of the unstable planetary boundary layer', *J. Atmos. Sci.*, **31,** 1297–1307 (1974).
26. J. C. André, G. De Moor, P. Lacarrère, G. Therry and R. du Vachat, 'Modeling the 24 hour evolution of the mean and turbulent structures of the planetary boundary layer', *J. Atmos. Sci.*, **35,** 1861–1883 (1976).
27. J. W. Deardorff, 'Three-dimensional numerical study of the height and mean structure of a heated planetary boundary layer', *Boundary Layer Meteorol.*, **7,** 81–106 (1974).

28. J. C. Wyngaard and O. R. Cote, 'The evolution of a convective planetary boundary layer—a higher-order-closure model study', *Boundary Layer Meteorol.*, **7**, 289–308 (1974).
29. W.-Y. Sun and Y. Ogura, 'Modeling the evolution of the convective planetary boundary layer', *J. Atmos. Sci.*, **37**, 1558–1572 (1980).